

## Global Multiscale Evaluation of Satellite Passive Microwave Retrieval of Precipitation during the TRMM and GPM Eras: Effective Resolution and Regional Diagnostics for Future Algorithm Development

CLÉMENT GUILLOTEAU AND EFI FOUFOULA-GEORGIU

*Department of Civil and Environmental Engineering, University of California, Irvine, Irvine, California*

CHRISTIAN D. KUMMEROW

*Department of Atmospheric Science, Colorado State University, Fort Collins, Colorado*

(Manuscript received 10 May 2017, in final form 1 August 2017)

### ABSTRACT

The constellation of spaceborne passive microwave (MW) sensors, coordinated under the framework of the Precipitation Measurement Missions international agreement, continuously produces observations of clouds and precipitation all over the globe. The Goddard profiling algorithm (GPROF) is designed to infer the instantaneous surface precipitation rate from the measured MW radiances. The last version of the algorithm (GPROF-2014)—the product of more than 20 years of algorithmic development, validation, and improvement—is currently used to estimate precipitation rates from the microwave imager GMI on board the GPM core satellite. The previous version of the algorithm (GPROF-2010) was used with the microwave imager TMI on board TRMM. In this paper, TMI-GPROF-2010 estimates and GMI-GPROF-2014 estimates are compared with coincident active measurements from the Precipitation Radar on board TRMM and the Dual-Frequency Precipitation Radar on board GPM, considered as reference products. The objective is to assess the improvement of the GPM-era microwave estimates relative to the TRMM-era estimates and diagnose regions where continuous improvement is needed. The assessment is oriented toward estimating the “effective resolution” of the MW estimates, that is, the finest scale at which the retrieval is able to accurately reproduce the spatial variability of precipitation. A wavelet-based multiscale decomposition of the radar and passive microwave precipitation fields is used to formally define and assess the effective resolution. It is found that the GPM-era MW retrieval can resolve finer-scale spatial variability over oceans than the TRMM-era retrieval. Over land, significant challenges exist, and this analysis provides useful diagnostics and a benchmark against which future retrieval algorithm improvement can be assessed.

### 1. Introduction

Observations of clouds and precipitation processes in the microwave (MW) domain from space have been performed since the late 1980s (Spencer et al. 1989). The launch of the Tropical Rainfall Measurement Mission (TRMM) satellite in 1997, carrying a Precipitation Radar (PR) along with the passive TRMM Microwave Imager (TMI), allowed an unprecedented amount of collocated MW multispectral atmospheric signatures and radar-derived vertical profiles of hydrometeor type

and density (Kummerow et al. 1998). This enabled the development of algorithms for the estimation of the surface (or near surface) precipitation rate from passive MW observations. Among these algorithms are the Goddard profiling algorithm (GPROF) and GSMaP, developed by NASA and JAXA, respectively (Kummerow et al. 2001; Aonashi et al. 2009). Other passive MW imagers similar to TMI have been sent into orbit since then: SSMI/S on board the DMSP platforms, AMSR on board Advanced Earth Observing Satellite-II (ADEOS-II), AMSR-E on board *Aqua*, Microwave Analysis and Detection of Rain and Atmospheric Structures (MADRAS) on board *Megha-Tropiques*, AMSR-2 on board *Global Change Observation Mission–Water (GCOM-WI)*, etc. In 2014, as a follow-up to TRMM, the Global Precipitation Measurement (GPM) *Core Observatory* satellite carrying the GPM

Denotes content that is immediately available upon publication as open access.

Corresponding author: Clément Guilloteau, cguillot@uci.edu

DOI: 10.1175/JHM-D-17-0087.1

© 2017 American Meteorological Society. For information regarding reuse of this content and general copyright information, consult the [AMS Copyright Policy \(www.ametsoc.org/PUBSReuseLicenses\)](http://www.ametsoc.org/PUBSReuseLicenses).

Microwave Imager (GMI) passive MW imager and the Dual-Frequency Precipitation Radar (DPR) was launched, making available a new set of collocated passive MW and radar observations of the atmosphere (Hou et al. 2014).

Several studies have evaluated the performance of satellite passive MW estimates of instantaneous precipitation rates by comparison with collocated radar or rain gauge data (e.g., Petty and Li 2013; Tang et al. 2014; Oliveira et al. 2015; Ebtehaj et al. 2016). These studies generally evaluate the ability of MW estimates to reproduce the statistical distribution of rain rates. They also quantify the similarity of MW estimates with the reference dataset through metrics such as mean squared difference (MSD) or the linear correlation coefficient.

Another important criterion one may consider in assessing the performance of the MW retrievals is their “effective resolution,” that is, the finest spatial scale at which they can accurately reproduce desired properties of precipitation fields. Determining the effective resolution of the surface rain rate estimated through the inversion of a multispectral signature is in fact far from trivial. Indeed, for a given spaceborne MW imager, the size of the footprint on the ground varies with the channel (Fig. 1). The scanning geometry and sampling rate combined with the satellite displacement during the measurement may lead to overlapping instantaneous fields of view for the low-frequency channels and to undersampling of the observed scene for the high-frequency channels (Kummerow et al. 1998; Petty and Bennartz 2017). The relative importance of each channel, and thus the effective resolution of the retrieval, may vary depending on parameters such as the surface type (Ferraro et al. 2013). Beyond the issue of the nominal resolution of each channel of the MW imagers, because of the indirect relation between observed radiances and the surface precipitation, the inversion is always ambiguous, and the MW signal may not contain sufficient information to resolve the finescale variability. Thus, the computation method used to deduce the surface precipitation rate from the measured MW radiances may induce a filtering effect or generate “computational noise” affecting the effective resolution of the estimate.

The above issues limit the classical point-to-point or pixel-to-pixel comparison with a reference dataset and calls for developing validation methods and metrics that compare the multiscale spatial structure and geometrical properties of the retrieved precipitation fields. Object-based approaches have been proposed to handle this issue (e.g., Nesbitt et al. 2006; Aghakouchak et al. 2011; Demaria et al. 2011). Objects are defined as contiguous areas with precipitation intensity above a given threshold. One can consider the number of objects, their

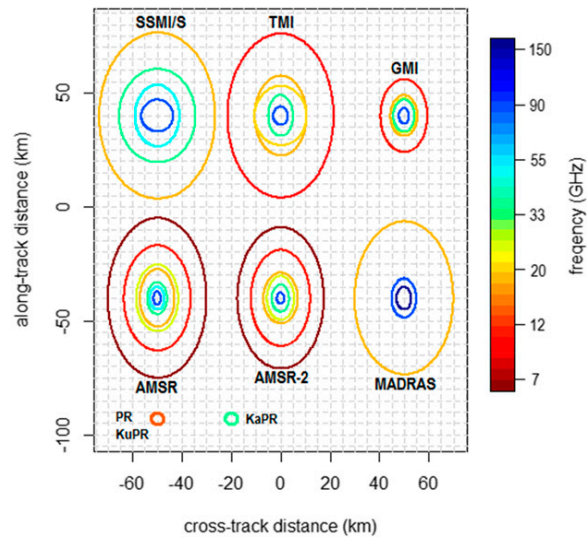


FIG. 1. Footprints on the ground ( $-3$  dB) of several spaceborne MW imagers compared with the footprints of the PR on board TRMM and the Ku PR and Ka PR on board GPM.

size, their convexity or compactness, etc., and evaluate the ability of MW estimates to preserve these characteristics. To comprehensively assess the ability of the estimates to reproduce precipitation patterns, the objects’ statistics must be computed with multiple thresholds, covering the whole range of possible precipitation intensities. These methods may be computationally intensive and lead to a large amount of computed parameters to be interpreted.

We propose here to use a spatial multiscale decomposition of the retrieved precipitation fields to assess the ability of MW-based methods to reproduce the spatial patterns of precipitation at various scales. A two-dimensional discrete orthogonal Haar wavelet decomposition is used to perform the analysis. It allows characterizing specifically each scale of variation of the precipitation fields in a nonredundant way. Wavelets being differential operators result in wavelet coefficients representing the local spatial gradients (or fluctuations) of precipitation fields at various scales. The orthogonal wavelet decomposition erases the spatial correlation of the analyzed signal, that is, the wavelet coefficient fields are spatially uncorrelated even if the original signal is spatially correlated. Wavelet filtering also removes possible nonstationarities in the original fields (in the case of the discrete Haar wavelet, it removes piecewise constant-level trends), rendering statistical interpretations more meaningful. Wavelets have been used successfully to characterize the spatial structure of the precipitation fields and the dependence of local precipitation rates on their surroundings (e.g., Kumar and Foufoula-Georgiou 1994, 1997).

Using a discrete orthogonal wavelet basis, which is a reconstructive basis, leads to a nonparametric reversible decomposition by which all the information contained in the original signal is contained in the wavelet coefficients. In this paper, MW estimates from TMI and GMI based on two different versions of the GPROF algorithm are compared with radar data in the wavelet domain. A wavelet spectral analysis is also performed by computing second-order statistics of the wavelet coefficients, to assess how the energy (spatial variance) of the signal is distributed across scales.

The main objective of this study is to assess the improvement in retrieval of instantaneous precipitation rates allowed by the last version of GPROF with the 13 channels of GMI compared to the TRMM-era version of the algorithm with the 9 channels of TMI. The smaller footprint of GMI compared with TMI (Fig. 1) is expected to allow resolving of precipitation structures at finer scales. However, the effective resolution as defined herein is a result of not only the nominal resolution of the instrument, but also of the information content of each MW channel and the ability of the retrieval algorithm to accurately interpret this information to reproduce the precipitation spatial variability and structure at fine scales. The MW estimated precipitation rates from TMI and GMI are compared to the precipitation rates measured by the PR on board TRMM and the DPR on board GPM, respectively. The radar-derived precipitation rates are considered an accurate enough reference product for the evaluation of the MW estimates, meaning that the radar retrieval error is considered negligible relative to the MW error. Besides, the regional discrepancies revealed by our analysis can always be assessed in the context of possible errors stemming from regional variations in the accuracy of the radar estimates. The potential inaccuracies in the radar estimates are discussed in the last section of this paper.

The article is organized as follows. The passive MW and radar datasets are presented in section 1. Section 2 is dedicated to the evaluation methodology relying upon the wavelet transform. In section 3, results are presented, first with an illustrative case study and then at a global scale with multiyear statistics. Section 4 discusses the results.

## 2. Data

### a. TRMM era: 6 years of TMI estimates collocated with PR observations

The PR on board the TRMM satellite produced measurements of the instantaneous surface rain rate under the track of the satellite from 1997 to 2015, at 13.8 GHz

(Ku band), with a 5-km horizontal resolution. The swath width of the radar is 245 km. The wider swath (880 km) of the TRMM Microwave Imager (TMI) encompasses the swath of the PR, allowing collocated observations. Here, 6 years (2002, 2005, 2008, 2011, 2012, and 2013) of retrieved surface rain rates derived from TMI through GPROF-2010 (product 2A12v7; TRMM 2011a) are compared with the surface rain rates from the PR (product 2A25v7; TRMM 2011b). For the comparison, TMI-GPROF estimates are projected on the 5-km grid of the 2A25v7 product using a nearest neighbor interpolation. It is to be noted that the computation schemes of GPROF-2010 are different over land and oceans. Over oceans, a Bayesian inversion scheme is used to retrieve the most probable hydrometeor profiles from a database made of 65 million coincident TMI and PR observations. Over land, stratiform and convective precipitation areas are first delimited using a scattering index. For each type of precipitation, an empirical relationship between precipitation rate and 85-GHz brightness temperatures is used (Kummerow et al. 2015; Petković and Kummerow 2017).

### b. GPM era: 3 years of GMI estimates collocated with Ku-PR observations

The equivalent of the 2A12 product for the GPM era is the experimental 2A-GPROF-GMI product, obtained by the inversion of the GMI spectral signatures with the new GPROF-2014 algorithm (GPM Science Team 2016a). For GPROF-2014, the same Bayesian scheme is used over land and oceans (Kummerow et al. 2015). Over oceans, the same database as in GPROF-2010 is used. Over land a database of coincident ground radar observations in North America and simulated radiances (from SSMI/S observations) is used. The GMI-GPROF estimates are collocated with the surface precipitation rates from the Ku-PR (lowest frequency of the DPR; GPM Science Team 2016b). The Ku PR on board GPM has the same characteristics as the TRMM PR. The measurements in the Ka band are not used in this study to ensure consistency of the reference datasets for the TRMM and GPM eras and because of the reduced swath width of the Ka PR (120 km only). We consider here 3 years of data, from March 2014 to March 2017. The GMI-GPROF estimates are projected on the Ku-PR 5-km grid for the comparison.

## 3. Methodology

### a. Motivation

Let  $R_{MW}(x, y)$  denote the passive MW retrieved field we want to evaluate and  $R_R(x, y)$  denote the radar field (Fig. 2), considered here as the reference, that is,

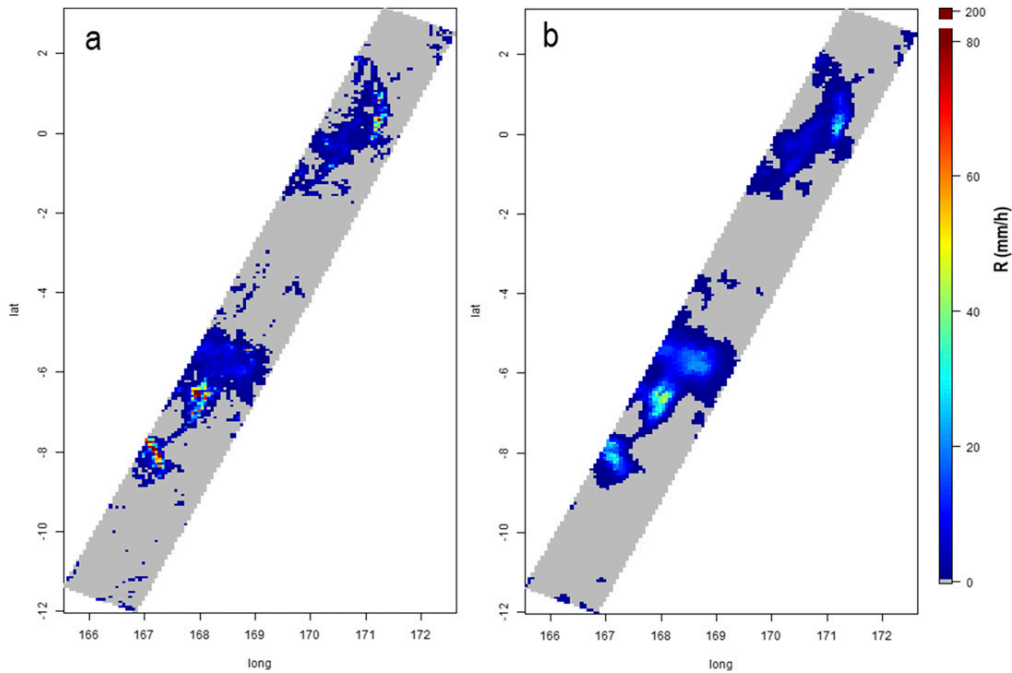


FIG. 2. Collocated radar and passive MW retrievals over the tropical Pacific Ocean at 1530 UTC 15 Nov 2015. (a)  $R_R(x, y)$ , precipitation rates retrieved by the Ku PR and (b)  $R_{MW}(x, y)$ , precipitation rates retrieved from GMI radiances using the GPROF-2014 algorithm.

$R_R(x, y) = R_{ref}(x, y)$ . The classical approach to evaluate  $R_{MW}$  would be to compare it to  $R_R$  pixel by pixel and compute scoring metrics such as the linear correlation coefficient and the mean squared difference. Doing so with the rain rates in the two images shown in Fig. 2, we obtain a correlation coefficient of 0.58 and a root-mean-square difference of  $7 \text{ mm h}^{-1}$ . This approach is adapted when one seeks to characterize a retrieval error that is stationary, independent of the reference rain rate  $R_{ref}(x, y)$ , and spatially uncorrelated, that is, an additive white noise:

$$R_{MW}(x, y) = R_{ref}(x, y) + \varepsilon(x, y), \quad (1)$$

where  $\varepsilon$  is a zero-mean random error. With this model,

$$\text{var}(R_{MW}) = \text{var}(R_{ref}) + \text{var}(\varepsilon), \quad (2)$$

where  $\text{var}()$  denotes the population variance. Unfortunately, this simple error model is not fit to characterize some aspects of the errors of passive MW estimates of precipitation. The error may actually be a complex combination of several types of errors such as instrumental noise, location error due to inaccurate pointing or parallax shift, nonlinear effects from inhomogeneous beam filling, filtering effects induced by the signal processing and computation method, etc.

In particular, assuming a spatially uncorrelated error is not reasonable. Many studies have also shown that the error actually is dependent on  $R_{ref}$ , which is itself a spatially correlated field (Hossain and Anagnostou 2006; Hossain and Huffman 2008; Aghakouchak et al. 2010; Kirstetter et al. 2013a). The error may also depend on other spatially correlated environmental parameters such as the surface MW emissivity. Passive MW retrieval is generally more challenging over land than over oceans because of the spatial and temporal heterogeneity of land surface emissivity and because the overland radiative signature of precipitation is fundamentally weaker and less direct when viewed against a high emissivity background. The question of error space-time correlation is of prime importance when the retrieved precipitation is to be combined with other estimates from ground or spaceborne instruments to compute multisensor estimation products or with modeled variables in a data assimilation scheme. The degree of spatial and temporal correlation also drives the rate at which the error variance decreases through spatial and temporal aggregation.

Passive MW retrieval methods such as GPROF rely on the inversion of a multispectral MW signature to infer the surface precipitation rate. These methods are generally designed to minimize a quadratic cost

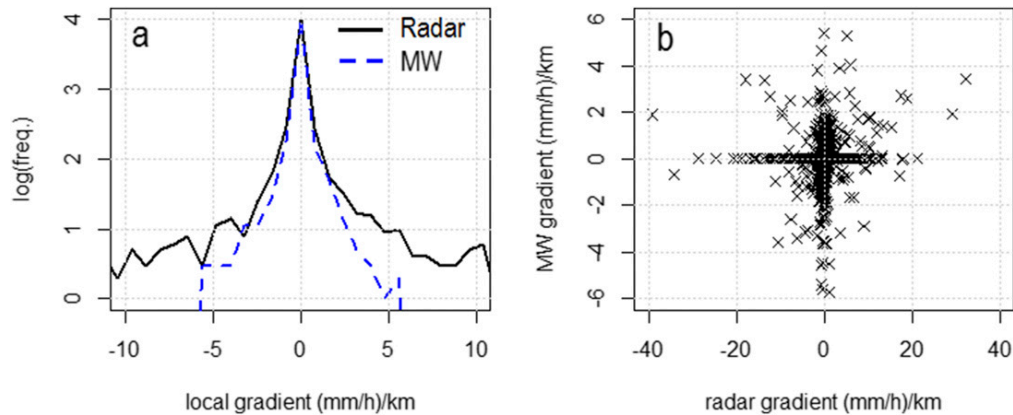


FIG. 3. Comparison of the gradients of the radar and passive MW precipitation fields displayed in Fig. 2. (a) Probability distribution of radar and MW spatial gradients revealing the smoother structure of the MW retrievals (lower gradients) and (b) scatterplot of MW gradients against radar gradients, revealing that gradients are uncorrelated. Gradients are computed along track as the difference of two adjacent pixels. Pixel resolution is 5 km. The linear correlation coefficient between passive MW and radar gradients is 0.085.

function—for example, the mean squared error (MSE)—or to provide the most likely rain rate given the observed parameters. Minimum MSE methods, Bayesian or empirical Bayesian methods such as the maximum likelihood, maximum a posteriori, best linear unbiased estimator, etc., tend to produce smooth estimates, discarding the extreme values (DeGroot 2004; Carroll et al. 2006; Buzas et al. 2014; Foufoula-Georgiou et al. 2014). In that case, the variance of the estimates is always smaller than the variance of the reference rain rates, which is inconsistent with the additive random error model [Eq. (2)]. These smooth estimates are in fact affected by a conditional systematic bias (Ciach et al. 2000; Kirstetter et al. 2013a), that is, the error necessarily depends on the reference rain rate. This smoothing of the rain rates naturally leads to a smoothing of the spatial gradients. The smoothing effect on the gradients is complex as gradients at different scales may be affected differently. Therefore, the effect on the effective resolution is not trivial. As an illustration, Fig. 3 shows the distribution of local gradients computed as the differences between two adjacent pixels (whose centers are 5 km apart), for the fields  $R_{MW}(x, y)$  and  $R_R(x, y)$  displayed on Fig. 2. The gradients of  $R_R$  have a wider distribution with more frequent extreme values compared to  $R_{MW}$ . Moreover, a very low correlation, 0.085, is found between the MW and radar gradients (to be compared with the 0.58 correlation coefficient for the precipitation rates themselves), showing that the fine-scale spatial features of the radar field are not reproduced by the MW estimate.

The correlation coefficient and MSD between the precipitation rates  $R_{MW}(x, y)$  and  $R_R(x, y)$ , as pointwise

or pixelwise metrics fail to reveal information about how well the spatial organization of the precipitation fields is captured in the retrieval and also do not provide information on the spatial structure of the retrieval error. Instead of quantifying absolute rain intensity, the wavelet coefficients represent the local differences of intensity at various scales. Thus, they quantify the spatial structure of precipitation fields, and therefore, correlation coefficients and MSD computed on the wavelet coefficients at each scale provide more specific information than the correlation coefficients and MSD of rain rates. In addition, because the wavelet coefficients are spatially uncorrelated, there is no ambiguity in the interpretation of their variance or covariance.

#### b. Implementation

The two-dimensional discrete Haar wavelet transform used in this study is an orthogonal decomposition, decomposing a field into series of wavelet coefficients encoding the spatial variations (i.e., gradients) of the field at various scales (Mallat 2008; Kumar and Foufoula-Georgiou 1993). While any orthogonal wavelet basis may theoretically be used, the Haar wavelet offers simplicity in interpretation, as the Haar wavelet coefficients can be interpreted in terms of simple finite differences and the smoothing function associated with the Haar wavelet as simple window averaging at different scales.

Figure 4 illustrates the discrete orthogonal decomposition of the two-dimensional MW precipitation field  $R_{MW}(x, y)$  with the Haar wavelet. At the first level of the decomposition, the field is decomposed into four components: three series of wavelet coefficients denoted as  $R'_{MW,1,k}(x, y)$  with  $k = \{1, 2, 3\}$ , and one series of

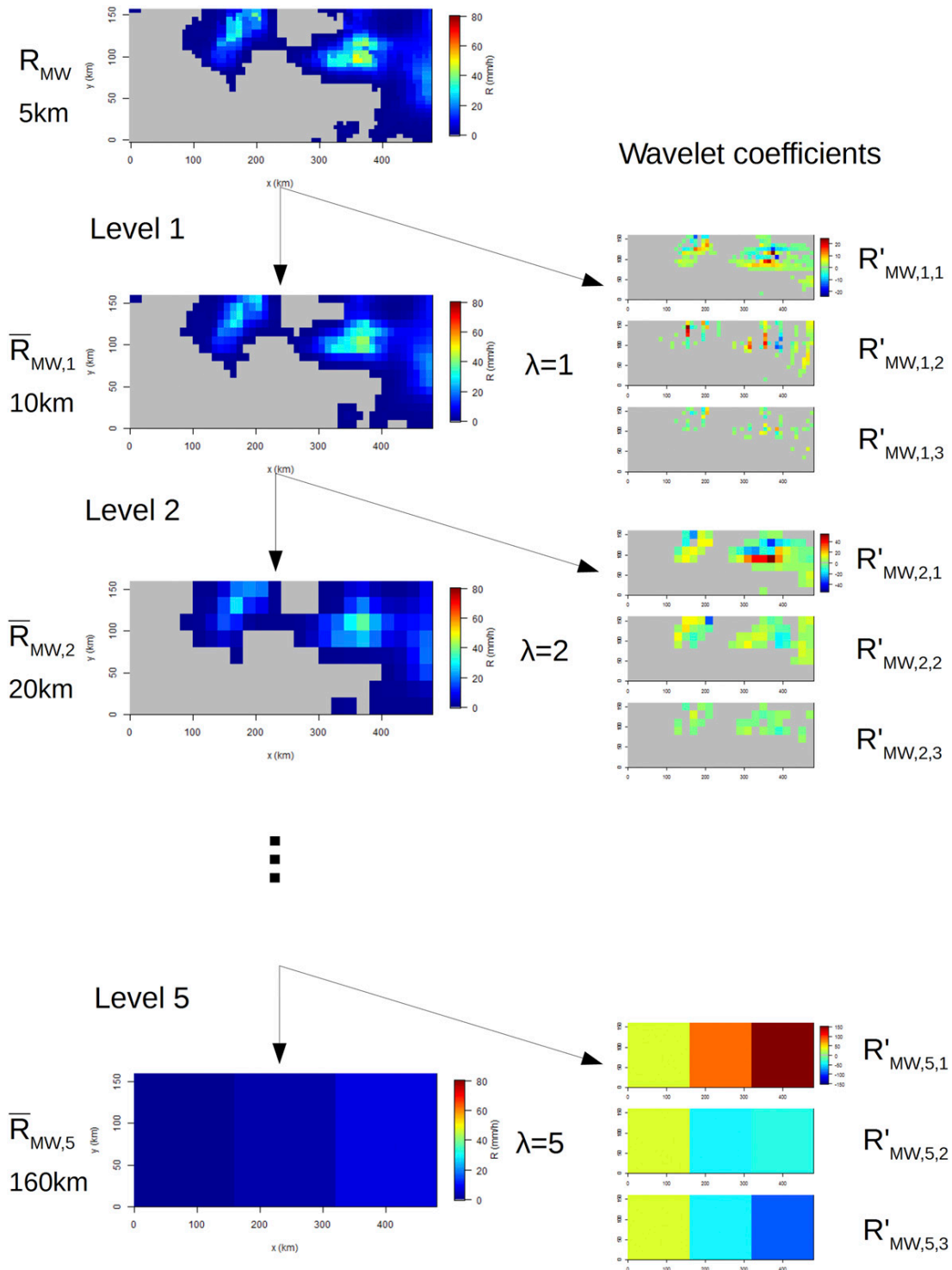


FIG. 4. Five-level discrete wavelet decomposition of the passive MW fields  $R_{MW}(x, y)$  displayed in Fig. 2. The top-left panel shows the original precipitation field at 5-km resolution. The other left panels show the low-pass coefficients  $\bar{R}_{MW,\lambda}(x, y)$ . The wavelet coefficients at various levels of decomposition are displayed in the right panels. The scales  $\lambda = 3$  and  $\lambda = 4$  are not displayed. The decomposition is performed using the Haar wavelet.

low-pass (LP) coefficients denoted as  $\overline{R_{MW,1}}(x, y)$ . The wavelet coefficients  $R'_{MW,1,k}(x, y)$  are kept and the LP component  $\overline{R_{MW,1}}(x, y)$  is further decomposed into  $R'_{MW,2,k}(x, y)$  with  $k = \{1, 2, 3\}$  and  $\overline{R_{MW,2}}(x, y)$  at the next level of decomposition (level two). This decomposition is performed for five levels in our case. Thus, at each level (scale), three sets of wavelet coefficients  $R'_{MW,\lambda,k}(x, y)$  complement a set of LP coefficients  $\overline{R_{MW,\lambda}}(x, y)$ , where  $k = \{1, 2, 3\}$  and  $\lambda$  is the scale index. The three sets of wavelet coefficients encode the variations of the field in three directions of the two-dimensional space and are necessary to comprehensively represent the spatial variability [see Eqs. (1)–(4) in Perica and Foufoula-Georgiou (1996) for interpretation of wavelet coefficients in terms of discrete approximations of spatial gradients]. In the present study, the three directions, imposed by the radars' scanning geometry and the satellite trajectory, are along track, cross track, and diagonal. Because the smoothing function associated with the Haar wavelet is a simple averaging operator,  $\overline{R_{MW,\lambda}}(x, y)$  is in fact no more than the original field coarsened at resolution  $L_\lambda = 2^\lambda L_0$ , where  $L_0$  is the original grid resolution. While the wavelet coefficients  $R'_{MW,\lambda,k}(x, y)$  are independent from one scale to another,  $\overline{R_{MW,\lambda}}(x, y)$  can be retrieved from  $\overline{R_{MW,\lambda+1}}(x, y)$  and  $R'_{MW,\lambda+1,k}(x, y)$ .

A necessary condition for the decomposition to be orthogonal and reconstructive is that the scale decomposition is dyadic, that is, the length scale  $L_\lambda$  is twice the length scale  $L_{\lambda-1}$  at the previous level of decomposition. The finest scale of the decomposition corresponds to the spatial sampling of the original field, 5 km in our case. The largest accessible scale is half the size (shortest dimension) of the original field, corresponding to the 245-km swath width of the radars in our case. Therefore, for this study, only five levels of decomposition are possible, and the spatial scales of 5, 10, 20, 40, and 80 km are labeled by the index  $\lambda = \{1, 2, \dots, 5\}$ . Finally, all the information contained in the original field  $R_{MW}(x, y)$  is retained in the LP field  $\overline{R_{MW,5}}(x, y)$ , and in the series of wavelet coefficients  $R'_{MW,\lambda,k}(x, y)$ , with  $\lambda = \{1, 2, \dots, 5\}$ . In the following,  $\overline{R_{MW,5}}$ , which is  $R_{MW}$  coarsened at the 160-km resolution, is simply noted as  $\overline{R_{MW}}$ . An identical decomposition is applied on the radar field  $R_R(x, y)$  to allow the multiscale comparison of the two fields.

Computing the energy (sum of squared values) of the wavelet coefficients at each scale results in the wavelet energy spectrum, which captures the fraction of the total energy of the signal contributed by each scale. Indeed, with the Haar orthogonal wavelet decomposition being energy conservative, the total energy of the signal is equal to the sum of the energy of its wavelet and LP coefficients:

$$\sum_{x,y} R_{MW}^2(x, y) = \sum_{x,y} \overline{R_{MW}^2}(x, y) + \sum_{\lambda=1}^5 \sum_{k=1}^3 \sum_{x,y} R_{MW,\lambda,k}^2(x, y). \quad (3)$$

The collocated wavelet coefficients  $R'_{MW,\lambda,k}(x, y)$  and  $R'_{R,\lambda,k}(x, y)$  are compared at each scale  $\lambda$ . From Eq. (3) we can see that the wavelet decomposition allows us to quantify the contribution of each scale to the total energy of a field. Similarly, by computing the squared difference and the covariance between the wavelet coefficients  $R'_{MW,\lambda,k}(x, y)$  and  $R'_{R,\lambda,k}(x, y)$ , we can quantify the contribution of each scale to the squared difference and covariance between  $R_{MW}(x, y)$  and  $R_R(x, y)$ .

The scoring metrics used to quantify the similarity of the wavelet coefficients  $R'_{MW,\lambda,k}(x, y)$  and  $R'_{R,\lambda,k}(x, y)$  at each scale, and thus assess the effective resolution of the MW retrieval, are the coefficient of linear correlation and the Nash–Sutcliffe (NS) efficiency coefficient. The NS efficiency is a normalized measure of the MSE, ranging from  $-\infty$  to 1, and accounting for the variance of the reference signal:

$$NS(R'_{MW,\lambda,k}, R'_{R,\lambda,k}) = 1 - \frac{\sum_{x,y} [R'_{MW,\lambda,k}(x, y) - R'_{R,\lambda,k}(x, y)]^2}{\sum_{x,y} \{R'_{R,\lambda,k}(x, y) - E[R'_{R,\lambda,k}]\}^2}, \quad (4)$$

where  $E[\ ]$  denotes the expected value. Note that, at any scale, the expected value of the wavelet coefficients  $E[R'_{\lambda,k}]$  is zero, and thus the energy of the wavelet coefficients is proportional to their variance. An NS efficiency equal to one indicates that the evaluated estimate is identical to the reference. A negative NS efficiency coefficient of the wavelet coefficients indicates that the precipitation variability signal is dominated (in terms of variance) by noise at the corresponding scale. We consider here that the spatial variability of precipitation at scale  $\lambda$  is effectively resolved if the NS efficiency of  $R'_{MW,\lambda,k}(x, y)$  compared to  $R'_{R,\lambda,k}(x, y, i)$  is above 0.5, that is, the signal-to-noise ratio is greater than 2:1. Thus, we can determine the effective resolution as the smallest scale above which the spatial variability of precipitation is effectively retrieved. In this study, the dyadic decomposition allows us to determine a range of scales within which the effective resolution lies. When the larger accessible scale (80 km with the dataset used here) is not resolved, we can only assess that the effective resolution is larger than this scale.

Although one could study independently the three directional wavelet components  $R'_{\lambda,1}(x, y)$ ,  $R'_{\lambda,2}(x, y)$ , and  $R'_{\lambda,3}(x, y)$  encoding the along-track, cross-track, and diagonal spatial variations, we note that these directions

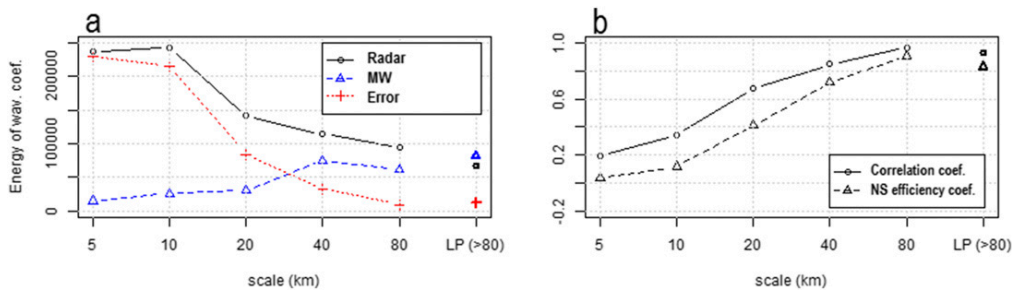


FIG. 5. Multiscale comparison of microwave  $R_{MW}$  and radar fields  $R_R$  displayed in Fig. 2. (a) Wavelet energy spectra of  $R_R$  (circles),  $R_{MW}$  (triangles), and Error = ( $R_{MW} - R_R$ ) (crosses). (b) Correlation coefficient between the wavelet coefficients  $R'_{MW,\lambda}$  and  $R'_{R,\lambda}$  and NS efficiency coefficient (triangles), as function of scale. In both plots, the rightmost symbols depict the values corresponding to the LP fields, that is, scales larger than 80 km. The energy deficiency and low correlation at scales finer than 40 km of the wavelet coefficients of the MW fields compared to the PR fields document the inability of the MW retrievals to reproduce small-scale features and establish 40 km as the “effective resolution” of the retrieval product.

are somewhat arbitrary as they depend on the orbital parameters of the satellite and do not have any specific meaning regarding the precipitation process itself. Moreover, these directions are not constant in any georeferenced coordinate system. For this reason, and to keep the evaluation concise, in the following, we chose to consider the three directions altogether and not to discriminate between the along-track, cross-track, and diagonal components.

#### 4. Results

##### a. Analysis of a case study

The purpose of this case study is to introduce and explain the significance of the metrics used for comparison. Here we compare the radar and MW fields shown in Fig. 2, corresponding to collocated GMI and Ku-PR observations over the Pacific on 15 November 2015. The wavelet and LP coefficients obtained from the decompositions of  $R_{MW}$  and  $R_R$  are displayed in Fig. 4. The corresponding wavelet energy spectra are displayed in Fig. 5a. The larger the spectral energy, the larger the spatial variability of the precipitation field at the corresponding scale. Comparing the  $R_{MW}$  and  $R_R$  wavelet spectra, it can be seen that the energy of the wavelet coefficients is lower for  $R_{MW}$  than for  $R_R$  at all scales between 5 and 80 km. This deficit of energy is particularly strong at the scales of 5, 10, and 20 km, illustrating the fact that the finescale spatial gradients are smoother in the  $R_{MW}$  field than in the  $R_R$  field. The radar sees sharper transitions, as it can detect small cells of very high rain intensity or identify small isolated rainy areas, while these are smoothed out in the MW estimates. The deficit of variability at 5 km, which was already revealed

in Fig. 3, is not surprising, considering that the  $R_{MW}$  original nominal resolution is 12.5 km, spatially interpolated to the 5 km grid of  $R_R$ . Nevertheless, the variability at scales of 10–80 km is also underrepresented in the MW field, demonstrating that the MW retrieval methodology is not able to reproduce the finescale spatial variability of the precipitation signal. Also, the fact that the variance of  $R'_{MW,\lambda}$  is consistently lower than the variance of the reference  $R'_{R,\lambda}$  at all scales confirms that the retrieval error cannot be described as an additive zero-mean random noise [Eqs. (1) and (2)], suggesting a systematic and scale-dependent conditional bias in the retrieved spatial gradients. On the contrary, for the LP component (which captures precipitation variability at scales coarser than 80 km), as  $\text{var}(\overline{R_{MW}}) > \text{var}(\overline{R_R})$ , the simple additive random error model may be adapted. These elements highlight the need of an orthogonal decomposition such as presented here for a more meaningful comparison.

As a consequence of the underrepresentation of finescale variability in the MW estimates, the energy of the error ( $R'_{MW,\lambda} - R'_{R,\lambda}$ ) increases and the correlation between  $R'_{MW,\lambda}$  and  $R'_{R,\lambda}$  decreases with finer scales (Fig. 5b). Specifically, at scales of 5–20 km, the energy of the error is of the same order as the energy of the reference signal  $R'_{R,\lambda}$ , leading to low NS efficiency, implying that the MW retrieval provides little information on the spatial variability of precipitation at those scales. From the NS efficiency of the wavelet coefficients, the effective resolution of  $R_{MW}$  is found to be between 20 and 40 km in this case study.

##### b. Global results during the TRMM era

Collocated  $R_{MW}(x, y)$  and  $R_R(x, y)$  precipitation fields derived respectively from TMI through the

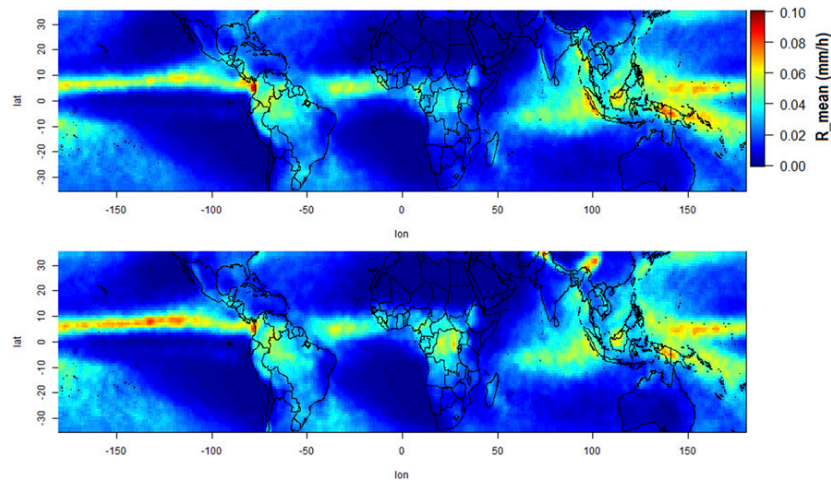


FIG. 6. Six-year,  $3^\circ \times 3^\circ$  average precipitation rates from the (top) PR and (bottom) TMI.

GPROF-2010 algorithm and from the TRMM-PR are compared in the wavelet domain. These observations correspond to more than 34 000 orbits completed by TRMM over 6 years (2002, 2005, 2008, 2011, 2012, and 2013). To perform regionalized analyses, the tropics ( $35^\circ\text{N}$ – $35^\circ\text{S}$ ) are divided into  $3^\circ \times 3^\circ$  grid cells. In each cell, for each TRMM overpass, the five-level, two-dimensional Haar wavelet decomposition of the MW and radar fields is performed. The average number of TRMM overpasses per grid cell during the six years is about 3000. Figure 6 shows the average observed precipitation rate. One can note the strong consistency between the MW estimates and radar observations in terms of the spatial patterns of the 6-yr mean at large scales. The only notable difference is the strong overestimation of the mean precipitation rate over the Himalayas for  $R_{\text{MW}}$  compared to  $R_{\text{R}}$ .

In all cells, the energy of the wavelet coefficients  $R'_{\text{MW},\lambda}(x, y)$  and  $R'_{\text{R},\lambda}(x, y)$  is computed at each scale  $\lambda$  and summed over all TRMM overpasses. The energy of the wavelet coefficients at all scales from 5 to 80 km, shown as percentage of the total energy of  $R_{\text{R}}(x, y)$  in each cell, is mapped in Fig. 7. It can be seen that, according to the radar, the contribution of the 5- and 10-km scales is strong everywhere, with those two scales generally accounting for more than 50% of the spatial variance in the radar fields. Over oceans, the MW estimate shows a high deficit of energy at the 5-, 10-, and 20-km scales compared to the radar. Once again, this result is not surprising, considering the way the passive MW retrieval is performed. The energy associated with the fluctuations at the 40- and 80-km scales and with the LP component is consistent between the radar and MW fields over oceans. Over land, the comparison shows much more

heterogeneous features. Over Amazonia, the MW and radar fields have a similar distribution of their spatial variability across scales (except at the 5-km scale, which for the MW field shows significantly less variability). Over central and western Africa, it appears that the MW overestimates the amplitude of spatial variations at scales of 20, 40, and 80 km. In this region, the variability of the LP term is also overestimated. Over the Himalayas, much larger energy is observed at all scales for the MW estimates than the radar fields, indicating that the MW retrieval strongly overestimates not only the mean intensity of precipitation (as shown by Fig. 7), but also the amplitude of its spatial variability at all scales.

Figure 8 shows the map of the correlation of wavelet coefficients  $R'_{\text{MW},\lambda}$  and  $R'_{\text{R},\lambda}$ , along with the map of the NS efficiency of the wavelet coefficients at each scale. Globally, the finer the scale, the lower the correlation and NS efficiency of the wavelet coefficients. Over the Himalayas and the Chilean Andes, the correlation and NS coefficients are low at all scales, as well as for the LP term. This indicates large-scale biases in the retrieval over these mountainous regions and erroneous spatial variability at all scales. In some continental regions, the NS efficiency coefficient is low while the correlation coefficient is relatively high. For example, over Sahelian Africa, the NS efficiency coefficient is negative at scales of 20, 40, and 80 km, while the correlation of wavelet coefficients is relatively high at the same scales. This demonstrates that in these regions, the form of the spatial variation of instantaneous precipitation at these scales is well captured by passive MW, but their amplitude is overestimated, as shown by the larger energy seen at these scales (Fig. 7). This feature had been previously identified by Petković and Kummerow (2017),

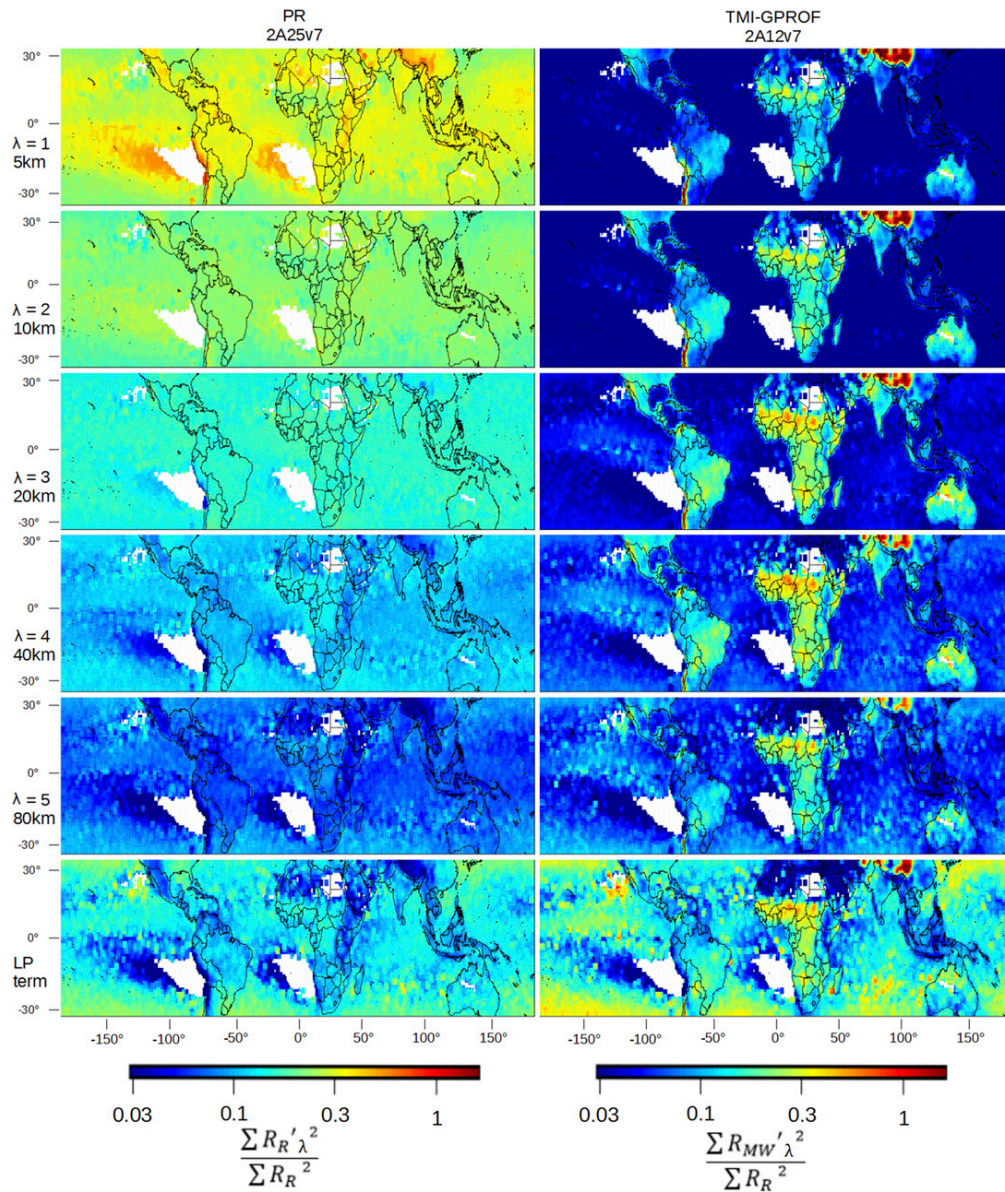


FIG. 7. Across-scale decomposition of the energy associated with the spatial variability of PR and TMI precipitation fields. The top five panels of each column show the energy of the wavelet coefficients (left)  $R'_{R,\lambda}$  and (right)  $R'_{MW,\lambda}$  at scales of 5–80 km, respectively. The bottom panels show the energy of the LP fields for  $\overline{R}_R$  on the left and  $\overline{R}_{MW}$  on the right. For each  $3^\circ \times 3^\circ$  cell, at each scale, the energy is computed over all TRMM overpasses during 6 years and normalized by the total energy of the PR field  $R_R$ . Areas with no plotted value are excluded, as the number of observed precipitation events is not sufficient to compute robust statistics in these areas. The contribution of the 5- and 10-km variability to the total variability is strong in the radar fields over land and oceans. In contrast, the 5- and 10-km scales barely contribute to the variability of the MW fields over oceans.

who explained it as a systematic overestimation of rain rates for deep convective systems that are predominant in this area.

Figures 9a–c displays the global wavelet spectra of  $R_R$  and  $R_{MW}$ , along with the spectrum of their difference,

over oceans and over land (excluding the Himalayas), as well as the regional spectra over the Himalayas. Over oceans, at all scales between 5 and 80 km, the energy of  $R'_{MW,\lambda}$  is lower than the energy of  $R'_{R,\lambda}$ , which indicates a conditional systematic bias and smoothing of the

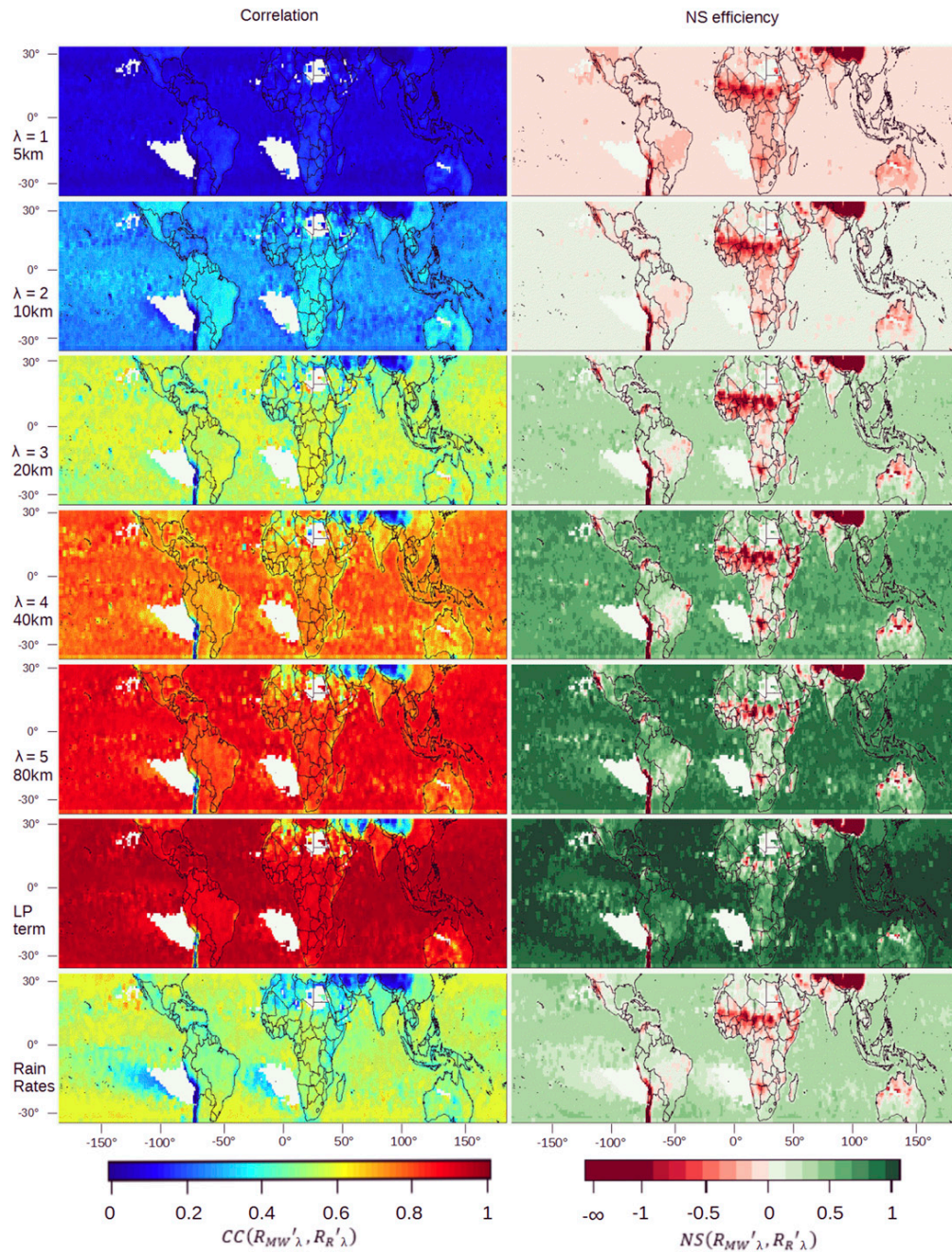


FIG. 8. Multiscale regionalized comparison of PR and TMI precipitation fields. (left) The top five panels show the correlation of the wavelet coefficients  $R'_{R,\lambda}$  and  $R'_{MW,\lambda}$  at scales of 5–80 km. The sixth panel shows the correlation of the LP coefficients  $\bar{R}_R$  and  $\bar{R}_{MW}$ . The bottom panel shows the correlation of the rain rates  $R_R$  and  $R_{MW}$ . (right) The top five panels show the NS efficiency of  $R'_{MW,\lambda}$  against  $R'_{R,\lambda}$  at scales of 5–80 km. The sixth panel shows the NS efficiency of  $\bar{R}_{MW}$  against  $\bar{R}_R$ , and the bottom panel shows the NS efficiency of  $R_{MW}$  against  $R_R$ . For each  $3^\circ \times 3^\circ$  cell, at each scale, the correlation and NS efficiency coefficients are computed over all TRMM overpasses during 6 years. Areas with no plotted value are excluded, as the number of observed precipitation events is not sufficient to compute robust statistics in these areas.

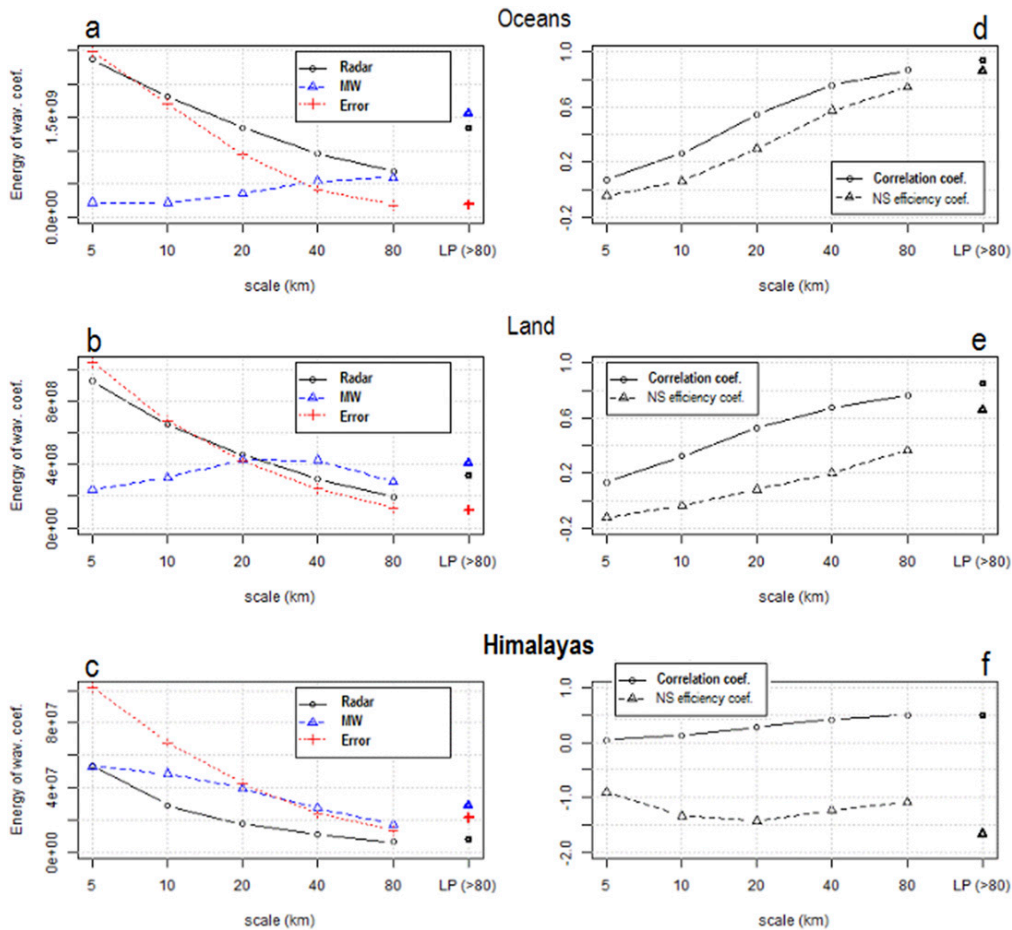


FIG. 9. Multiscale global comparison of TMI and PR precipitation fields. (left) As in Fig. 5a, but computed globally (between 35°N and 35°S) from 6 years of collocated TMI and PR observations over (a) oceans and (b) land and (c) at the regional scale over the Himalayas. (right) As in Fig. 5b, but computed globally (between 35°N and 35°S) from 6 years of collocated TMI and PR observations over (d) oceans and (e) land and (f) at the regional scale over the Himalayas. For the land statistics in (b) and (e), the Himalayan region is excluded. Over oceans the variance of the MW wavelet coefficients being lower than the variance of the radar wavelet coefficients indicates an error correlated to the reference field at scales finer than 80 km. For the LP fields,  $\text{var}(\overline{R}_{\text{MW}}) \approx \text{var}(\overline{R}_R) + \text{var}(\overline{\epsilon})$ , which is consistent with a random error independent from  $\overline{R}_{\text{ref}}$ .

finescale variability. For the LP term  $\overline{R}_{\text{MW}}$ , the random additive error model may be appropriate as  $\text{var}(\overline{R}_{\text{MW}}) \approx \text{var}(\overline{R}_R) + \text{var}(\overline{\epsilon})$ ; note that the variance of the LP error is low compared to the variances of  $\overline{R}_R$ .

Over land, the error appears to be much more complex, as the spatial variability is overestimated by the MW retrieval at scales of 40 and 80 km and underestimated at scales of 5 and 10 km. At the 20-km scale,  $R'_{\text{MW},\lambda}$  and  $R'_{R,\lambda}$  have about the same variance, but, from the correlation coefficient (Figs. 9d–f), it appears that only 50% of this variance is attributable to correctly capturing the localized variability, with the remaining 50% being attributable to random noise. At the 10- and

5-km scales, the variance of the error  $R'_{\text{MW},\lambda} - R'_{R,\lambda}$  is very high (higher than the variance of  $R'_{R,\lambda}$ ), leading to a negative NS efficiency (Figs. 9d–f). Note that the correlations are not significantly lower over land than over oceans, as one could have expected, indicating that the form of the spatial variations of precipitation rates over land is captured by the 85-GHz brightness temperature as effectively as over oceans through the combination of all channels. However, the NS efficiency is lower over land than over oceans, indicating erroneous estimation of the amplitude of the spatial variations.

Over the Himalayas, at all scales from 10 to 80 km, the energy of  $R'_{\text{MW},\lambda}$  is higher than the energy of  $R'_{R,\lambda}$ . The LP

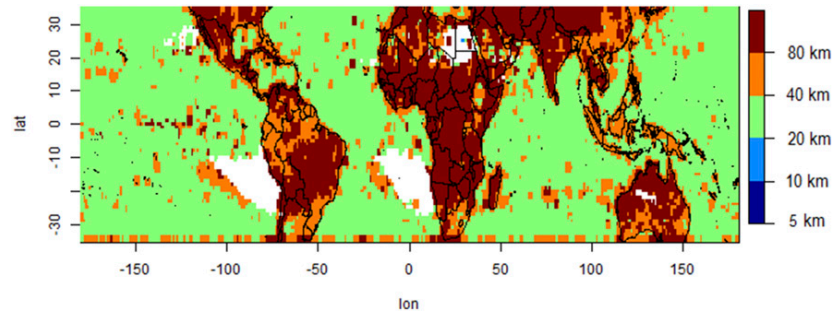


FIG. 10. Effective resolution of TMI-GPROF-2010 estimates. The effective resolution is computed from 6 years of collocated observations with the PR in each  $3^\circ \times 3^\circ$  cell.

term  $\overline{R_{MW}}$  also shows more energy than  $\overline{R_R}$ . The low correlations between  $\overline{R_{MW}}$  and  $\overline{R_R}$  and between  $R'_{MW,\lambda}$  and  $R'_{R,\lambda}$  at all scales indicate that the  $R_{MW}$  signal over the Himalayas is mostly noise, whose variance is larger than the variance of the precipitation signal. According to Petković and Kummerow (2017), this predominant noise is due to the indiscrimination between cold 85-GHz brightness temperatures coming from snow-covered areas and precipitation clouds. The wavelet analysis reveals that this noise is spatially correlated as it affects all scales of the signal.

From the wavelet decomposition the  $R_{MW}$  field can be reconstructed as linear combinations of the LP fields  $\overline{R_{MW}}$  and of the wavelet-encoded variations. Similarly, the correlation and MSD between  $R_{MW}$  and  $R_R$  are linear combinations of the correlations and MSD of the wavelet and LP coefficients. The last row of Fig. 8 shows the map of correlation and NS efficiency of precipitation rates  $R_{MW}$  against  $R_R$ . Figure 10 shows the effective resolution of the GMI-GPROF estimates, computed from 6 years of data, for each  $3^\circ \times 3^\circ$  cell. Over oceans, the effective resolution is generally between 20 and 40 km. Even if the effective resolution is also between 20 and 40 km in some continental areas, over land, the effective resolution is more often found to be coarser than 40 km and even coarser than 80 km in some regions.

### c. Global results during the GPM era

The same diagnostics used to analyze six years of collocated PR and TMI observations are applied on the 2014–17 collocated GMI and Ku-PR observations (more than 16000 GPM orbits). Rain rates are derived from GMI measured radiances through the GPROF-2014 algorithm. As for the TRMM era, the large-scale global patterns of the MW-derived mean intensity are very consistent with the radar estimates (Fig. 11). The overestimation over the Himalayas that characterized the TRMM-era retrievals (Fig. 6) does not appear anymore.

Figure 12 is the equivalent of Fig. 8 for the GPM era and shows the distribution of energy across scales for the MW and radar fields. Note that because of the reduced number of observations per  $3^\circ \times 3^\circ$  grid cell compared to the TRMM era (700 on average from the GPM era against 3000 for the TRMM era), the results show less spatial coherency, the “noisy” appearance of the maps being an effect of sample size. The orbit of GPM allows the observation of the regions between  $35^\circ$  and  $65^\circ$  of latitude, which was not observed by TRMM. As for TMI during the TRMM era, the GMI fields show less energy than the radar fields in the scales of 5, 10, and 20 km over oceans. Note that this deficit of energy is also observed over land while it was not the case during the TRMM era. This may result from the adoption of Bayesian retrieval scheme over land for the 2014 version of the GPROF algorithm, leading to smooth estimates both over land and oceans. The energy in scales of 40 and 80 km and in the LP term is consistent between the MW and radar fields, over land and oceans. Note that the LP term strongly contributes to energy of the MW and radar fields over medium- and high-latitude oceans. This reveals that over medium- and high-latitude oceans, precipitating systems tend to be dominated by large-scale features and be correlated over long distances, with relatively small finescale variability.

Figure 13 is the equivalent of Fig. 8 for the GPM era. As previously observed, globally, the finer the scale, the lower the correlation and NS efficiency. At all scales, the correlations between  $R'_{MW,\lambda}$  and  $R'_{R,\lambda}$  are significantly higher over oceans than over land. One will, however, note lower performance at all scales over the Southern Ocean below  $60^\circ\text{S}$ , which can be explained by the complex surface emissivity due to the presence of sea ice. Concerning the LP term, the correlation between  $\overline{R_{MW}}$  and  $\overline{R_R}$  is high everywhere, even over Chile and over the Himalayas. Figure 14 shows the average spectra computed over oceans and continents (excluding the Himalayas) and the regional spectra for the Himalayas.

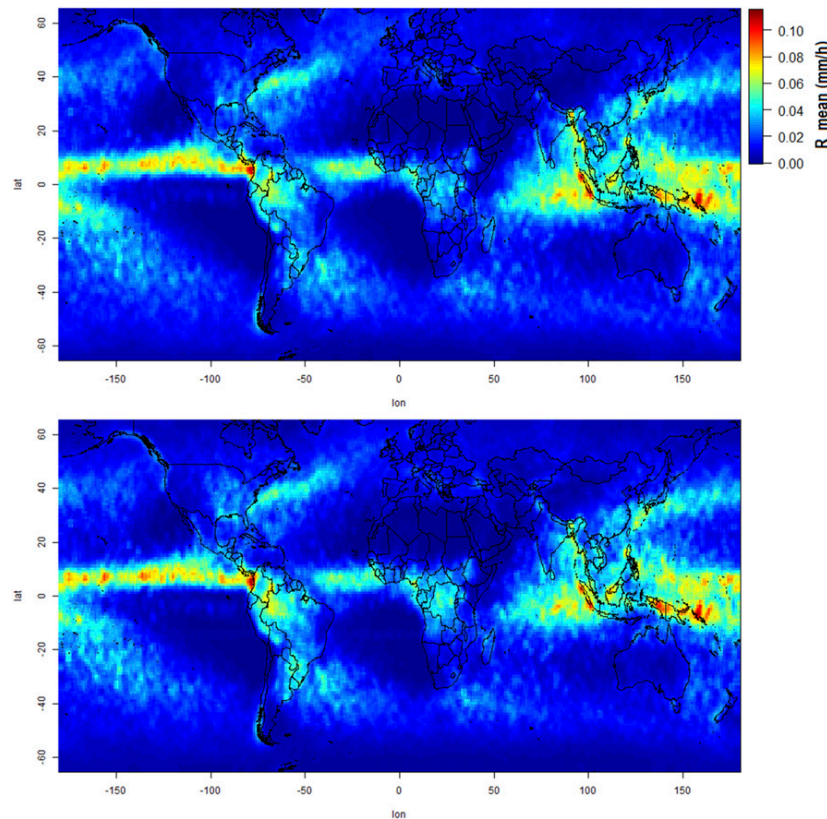


FIG. 11. Three-year,  $3^\circ \times 3^\circ$  average precipitation rates from the (top) Ku PR and (bottom) GMI.

Over oceans, the MW retrieval smooths spatial variations at scales of 5–40 km. For the 80-km scale and the LP term, the error is very low. The relative variances of  $\overline{R_{MW}}$  and  $\overline{R_R}$  and of the LP error indicate again that the LP error is random (i.e., independent from  $\overline{R_R}$ ). The correlation of MW and the radar wavelet coefficients at all scales are higher than during the TRMM era. The LP component of the MW and radar fields is also better correlated than during the TRMM era, indicating a better performance of GPM retrievals to accurately capture the precipitation variability at scales larger than 80 km.

Over land the error appears to be of the same type as over oceans: very little spatial variability is resolved for scales finer than 80 km (smooth spatial gradients), and unbiased estimates (random errors) are found for scales equal to or larger than 80 km. The relative variance of the LP error is higher over land than over oceans. Although the variance of  $R'_{MW,\lambda}$  has been reduced over land compared with the TRMM-era estimates, meaning smoother estimates and noise reduction, no improvement is noted in terms of correlation of the

wavelet coefficients, still implying a lack of ability to accurately resolve precipitation features at scales finer than 80 km. For example, over the Himalayas, the variations at scales finer than 80 km are essentially noise. However, contrary to the TRMM era, the correlation for the LP terms  $\overline{R_{MW}}$  and  $\overline{R_R}$  is relatively high (about 0.8), demonstrating the ability of GPM passive MW in capturing the form of spatial variations scales coarser than 80 km in a mountainous area (although the amplitude of these LP variations is overestimated).

The computed local effective resolution of 2014–17 GMI-GPROF-2014 estimates all over the globe is displayed in Fig. 15. The GMI estimates have an effective resolution between 10 and 20 km over most of the oceanic areas, which actually corresponds to the nominal resolution of the product (12.5 km). Although significant improvements in error reduction at the coarse scale are observed over land compared to the TRMM-era estimates, the effective resolution is still found to be coarser than 40 km over most of the continental areas for GMI estimates.

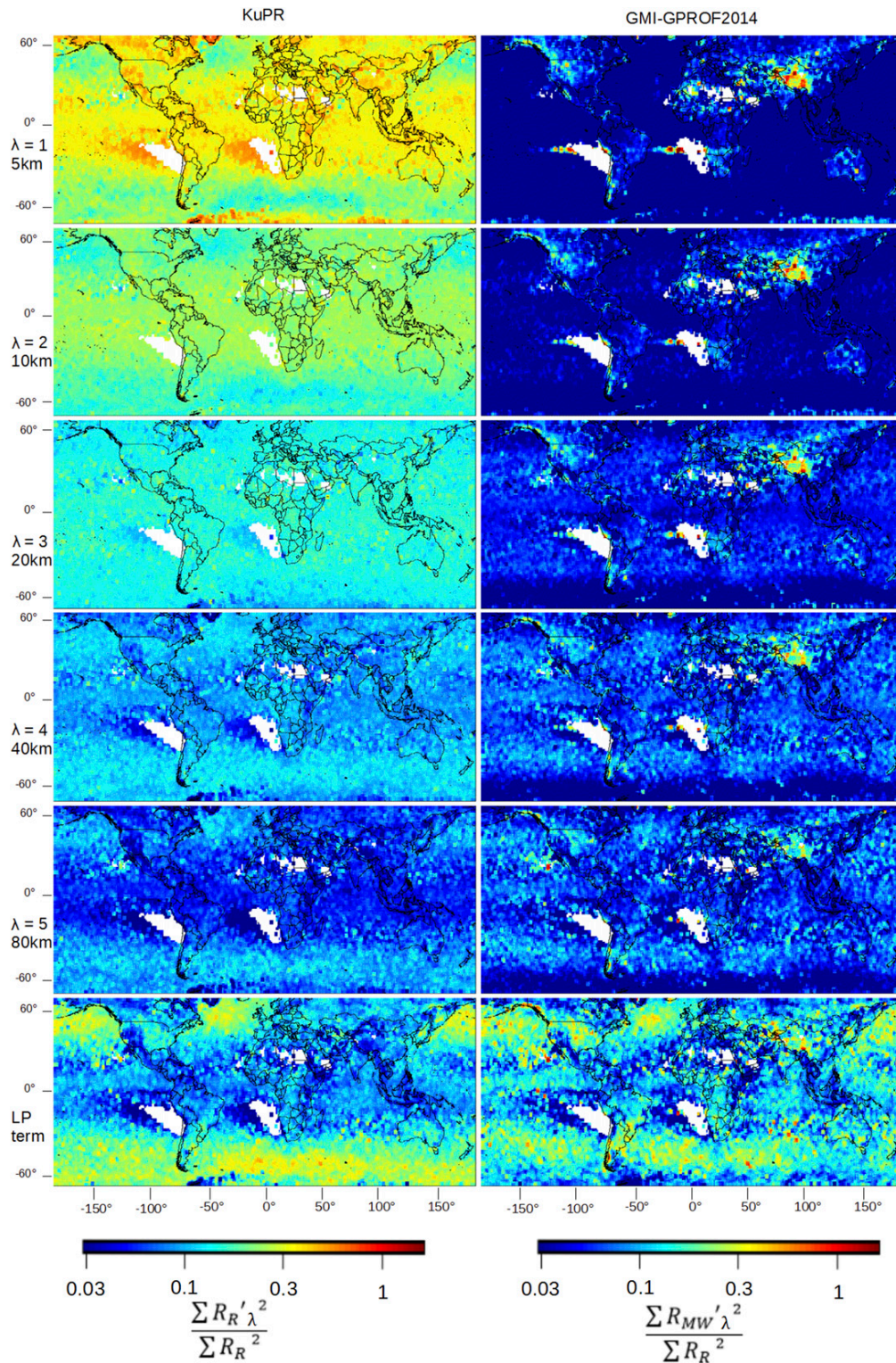


FIG. 12. Across-scale decomposition of the energy associated with the spatial variability of the Ku-PR and GMI precipitation fields. As in Fig. 7, but for the GPM era (from March 2014 to March 2017): (left) Ku-PR fields and (right) GMI fields. For each  $3^\circ \times 3^\circ$  cell area, at each scale, the energy is computed over all GPM overpasses during 3 years and normalized by the total energy of the Ku-PR field  $R_R$ .

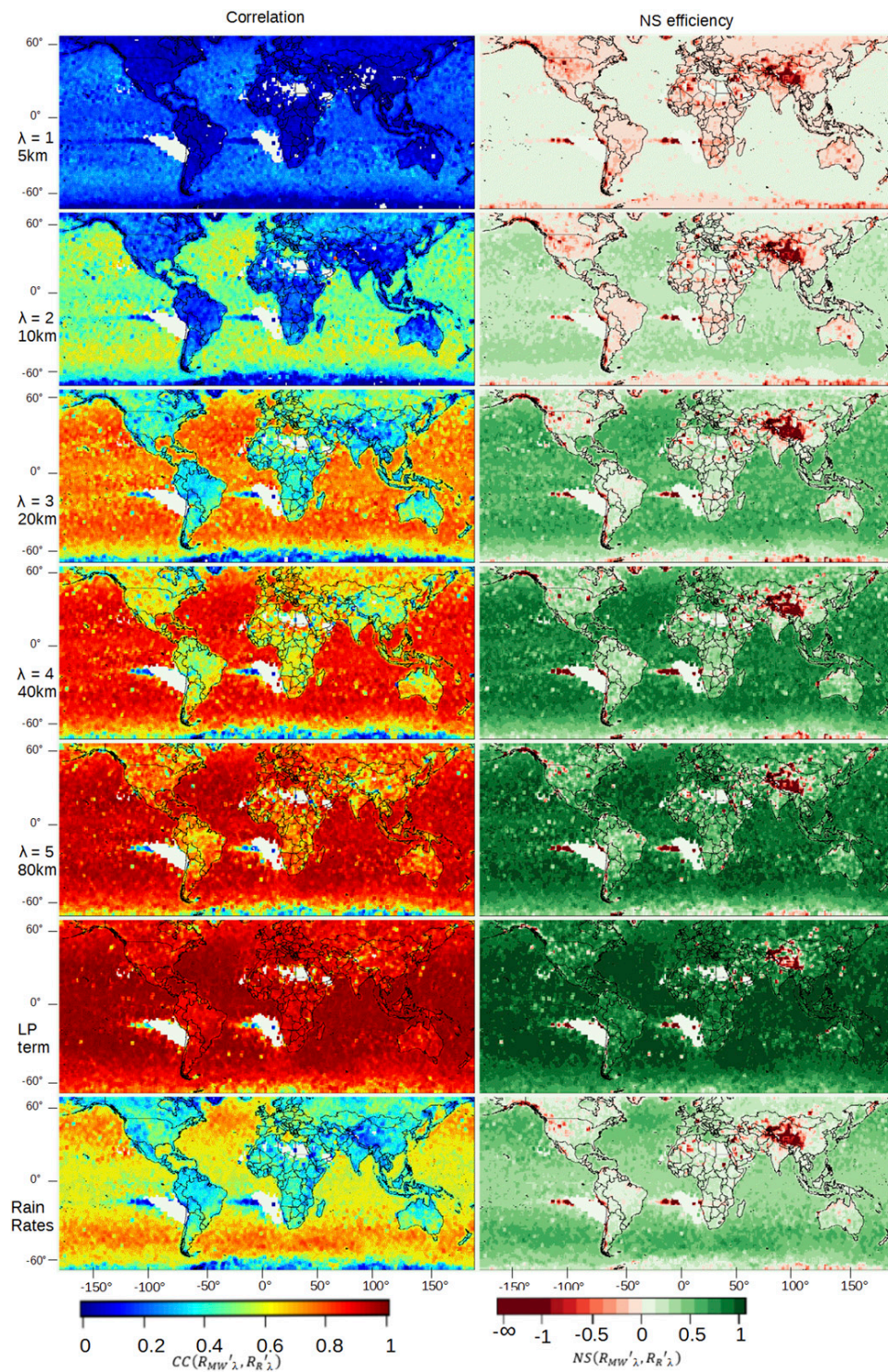


FIG. 13. Multiscale regionalized comparison of Ku-PR and GMI precipitation fields. As in Fig. 8, but for the GPM era (from March 2014 to March 2017).

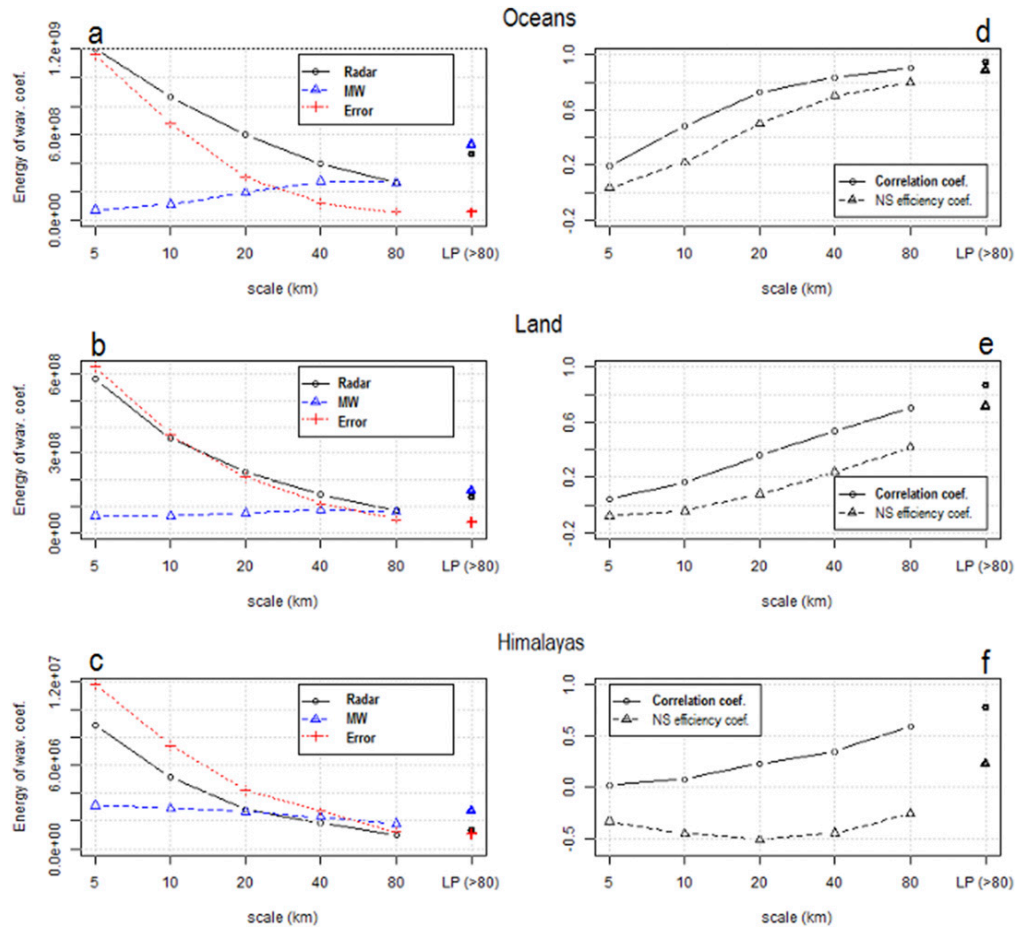


FIG. 14. Multiscale global comparison of GMI and Ku-PR precipitation fields. As in Fig. 9, but computed with 3 years of collocated GMI and Ku-PR observations over (a),(d) oceans; (b),(e) land; and (c),(f) the Himalayas. For the land statistics, the Himalayan region is excluded. The land and ocean statistics extend to the latitudes between 35°N(S) and 65°N(S) that were not observed during the TRMM era. Contrary to the TRMM era, the error structures are similar over land and oceans, consistent with the fact that the same Bayesian scheme is used over land and oceans during the GPM era.

**5. Conclusions**

The ability of passive MW precipitation retrievals to reproduce the spatial variability of precipitation fields at various scales is evaluated during the TRMM era and during the GPM era, seeking to quantify the improvement allowed by the enhanced instrumental capabilities of GPM and algorithmic developments. Instead of comparing the MW estimates with a reference dataset in terms of rain rates, our evaluation relies on comparing the wavelet coefficients resulting from a two-dimensional dyadic orthogonal wavelet decomposition of MW and radar precipitation fields. The wavelet methodology offers advantages as it filters out possible trends and nonstationarities in the original fields; it captures “edges,” that is, intensity contrasts due to local

precipitation features of different scales, and it renders the wavelet coefficient fields spatially and across-scale independent for more meaningful statistical analysis. Using the radar precipitation fields as the reference, our analysis allowed us to determine which scales of variability can be effectively retrieved through passive MW. The main findings are as follows:

- 1) Over oceans, rainfall variability down to spatial scales of 20–40 km is accurately retrieved from TRMM, while improvements down to scales of 10–20 km have been realized from GPM.
- 2) Over land, in most areas, only scales around 40–80 km or coarser are resolved for both the TRMM era and the GPM era. The adoption of the Bayesian retrieval over land for the GPM era led to smoother

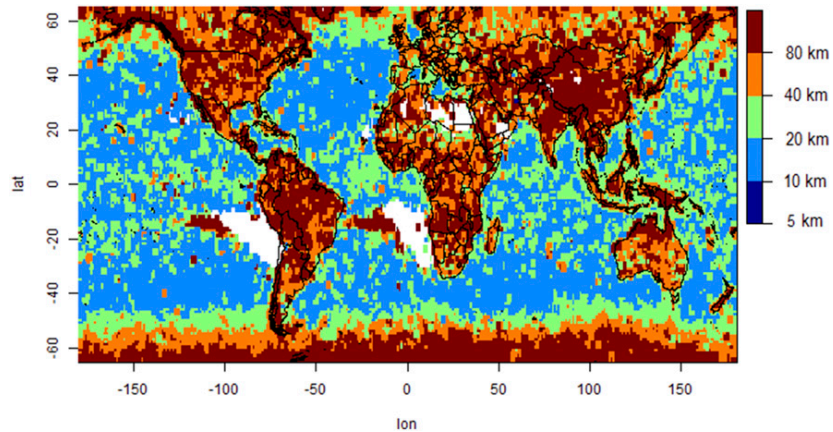


FIG. 15. Effective resolution of GMI-GPROF-2014 estimates. The effective resolution is computed from 3 years of collocated observations with the Ku PR in each in each  $3^\circ \times 3^\circ$  cell.

estimates. The magnitude of the finescale noise over land is reduced compared to the TRMM era, but the finescale spatial variability is still unresolved over land during the GPM era.

- 3) The spatial variability of precipitation rates at a given scale may not be resolved by the MW retrieval for two different reasons. First, they may be filtered out during the retrieval. In that case, the variance of the wavelet coefficients is low, and the information at the corresponding scale is missing. Second, they may be altered by noise. In that case, the wavelet coefficients have a high variance; they contain information, but this information appears to be unrelated to the precipitation process. These two cases may coexist at different scales and can hardly be represented by a unique error model.
- 4) The low-pass term representing the coarse scale (coarser than 80 km) spatial variations of the fields is well retrieved everywhere except over mountainous areas during both the TRMM and GPM eras.

The results help us better understand the scale dependence of the retrieval error. As expected, the finescale variability is generally less accurately retrieved than the large-scale variability. The exception is mountainous areas for which the retrieval of coarse-scale variability is also problematic. In most areas, the larger part of the error in MW rain rates comes from the underrepresentation of the finescale spatial variability (at scales finer than 40 km). A much smaller part comes from the error affecting the coarse-scale fields; this coarse-scale error has the characteristics of a random noise.

It must be noted that while GPROF-2014 retrieval over oceans has been developed in the continuity of GPROF-2010, over complex terrains it marks a deviation from previous versions, as GPROF-2014 is the first version of

GPROF implementing the Bayesian retrieval over land. As expected, the Bayesian retrieval produces smoother fields than the empirical relation used for the TRMM-era overland retrieval. The passive MW retrieval over land remains more uncertain than over oceans because of the heterogeneity of land surface emissivity. If the spatial variability at scales finer than 80 km is still hardly retrieved over land, the coarse-scale variability is well reproduced: coarse-scale correlations with radar are high everywhere, and except for mountainous areas, no large-scale systematic bias is noted. The next step in the ongoing development of the GPROF algorithm is the integration of coincident GMI and DPR observations in the database used for the retrieval.

In this paper, the radar precipitation fields from the PR on board TRMM and the DPR on board GPM are used as a reference. It is assumed that the radars are able to resolve precipitation spatial variability at scales down to 5 km. The radar products have been validated and calibrated regionally against ground radar data (Islam et al. 2012; Kirstetter et al. 2013b; Chen and Chandrasekar 2016). Nevertheless, part of the discrepancies between the passive MW and radar estimates may come from errors of the radar estimates. Frozen precipitation is known to be challenging for both radar and passive MW retrieval, which may explain part of the discrepancies over mountainous areas and high-latitude regions. Moreover, the effective resolution of the radar estimates is also eventually questionable, and an approach similar to the one presented here may be used to determine it.

*Acknowledgments.* This work was supported by the NASA Global Precipitation Measurement Program under Grant NNX16AO56G. The authors thank Dr. A. M. Ebtehaj, who performed the TMI-PR collocation

for the 2002–13 period. The wavelet decomposition procedure was implemented in R distributed under GNU General Public License, using the Waveslim 1.7.5 package (Whitcher 2015).

## REFERENCES

- AghaKouchak, A., A. Bárdossy, and E. Habib, 2010: Conditional simulation of remotely sensed rainfall data using a non-Gaussian v-transformed copula. *Adv. Water Resour.*, **33**, 624–634, doi:10.1016/j.advwatres.2010.02.010.
- , N. Nasrollahi, J. Li, B. Imam, and S. Sorooshian, 2011: Geometrical characterization of precipitation patterns. *J. Hydrometeorol.*, **12**, 274–285, doi:10.1175/2010JHM1298.1.
- Aonashi, K., and Coauthors, 2009: GSMaP passive microwave precipitation retrieval algorithm: Algorithm description and validation. *J. Meteor. Soc. Japan*, **87A**, 119–136, doi:10.2151/jmsj.87A.119.
- Buzas, J. S., L. A. Stefanski, and T. D. Tosteson, 2014: Measurement error. *Handbook of Epidemiology*, W. Ahrens and I. Pigeot, Eds., Springer, 729–765.
- Carroll, R. J., D. Ruppert, L. A. Stefanski, and C. M. Crainiceanu, 2006: *Measurement Error in Nonlinear Models: A Modern Perspective*. 2nd ed. Chapman & Hall/CRC Monographs on Statistics and Applied Probability, No. 105, CRC Press, 484 pp.
- Chen, H., and V. Chandrasekar, 2016: Validation of NASA's Global Precipitation Measurement mission with a high-resolution ground radar network. *URSI Asia-Pacific Radio Science Conf.*, Seoul, South Korea, IEEE, 836–839, doi:10.1109/URSIAP-RASC.2016.7601343.
- Ciach, G. J., M. L. Morrissey, and W. F. Krajewski, 2000: Conditional bias in radar rainfall estimation. *J. Appl. Meteor.*, **39**, 1941–1946, doi:10.1175/1520-0450(2000)039<1941:CBIRRE>2.0.CO;2.
- DeGroot, M. H., 2004: *Optimal Statistical Decisions*. John Wiley & Sons, 489 pp.
- Demaria, E. M. C., D. A. Rodriguez, E. E. Ebert, P. Salio, F. Su, and J. B. Valdes, 2011: Evaluation of mesoscale convective systems in South America using multiple satellite products and an object-based approach. *J. Geophys. Res.*, **116**, D08103, doi:10.1029/2010JD015157.
- Ebtehaj, A. M., R. L. Bras, and E. Foufoula-Georgiou, 2016: Evaluation of ShARP passive rainfall retrievals over snow-covered land surfaces and coastal zones. *J. Hydrometeorol.*, **17**, 1013–1029, doi:10.1175/JHM-D-15-0164.1.
- Ferraro, R. R., and Coauthors, 2013: An evaluation of microwave land surface emissivities over the continental United States to benefit GPM-era precipitation algorithms. *IEEE Trans. Geosci. Remote Sens.*, **51**, 378–398, doi:10.1109/TGRS.2012.2199121.
- Foufoula-Georgiou, E., A. M. Ebtehaj, S. Q. Zhang, and A. Y. Hou, 2014: Downscaling satellite precipitation with emphasis on extremes: A variational  $\ell_1$ -norm regularization in the derivative domain. *Surv. Geophys.*, **35**, 765–783, doi:10.1007/s10712-013-9264-9.
- GPM Science Team, 2016a: GPM GMI (GPROF) Radiometer Precipitation Profiling L2A 1.5 hours 13 km, V05. Goddard Earth Sciences Data and Information Services Center (GES DISC), accessed 20 March 2017, [https://disc.gsfc.nasa.gov/datasets/GPM\\_2AGPROFGPMGML\\_V05/summary](https://disc.gsfc.nasa.gov/datasets/GPM_2AGPROFGPMGML_V05/summary)
- , 2016b: GPM DPR Ku Precipitation Profile 2A 1.5 hours 5 km, V05. Goddard Earth Sciences Data and Information Services Center (GES DISC), accessed 20 March 2017, [https://disc.gsfc.nasa.gov/datasets/GPM\\_2AKu\\_V05/summary](https://disc.gsfc.nasa.gov/datasets/GPM_2AKu_V05/summary).
- Hossain, F., and E. N. Anagnostou, 2006: A two-dimensional satellite rainfall error model. *IEEE Trans. Geosci. Remote Sens.*, **44**, 1511–1522, doi:10.1109/TGRS.2005.863866.
- , and G. J. Huffman, 2008: Investigating error metrics for satellite rainfall data at hydrologically relevant scales. *J. Hydrometeorol.*, **9**, 563–575, doi:10.1175/2007JHM925.1.
- Hou, A. Y., and Coauthors, 2014: The Global Precipitation Measurement mission. *Bull. Amer. Meteor. Soc.*, **95**, 701–722, doi:10.1175/BAMS-D-13-00164.1.
- Islam, T., M. A. Rico-Ramirez, D. Han, P. K. Srivastava, and A. M. Ishak, 2012: Performance evaluation of the TRMM precipitation estimation using ground-based radars from the GPM validation network. *J. Atmos. Sol.-Terr. Phys.*, **77**, 194–208, doi:10.1016/j.jastp.2012.01.001.
- Kirstetter, P. E., N. Viltard, and M. Gosset, 2013a: An error model for instantaneous satellite rainfall estimates: Evaluation of BRAIN-TMI over West Africa. *Quart. J. Roy. Meteor. Soc.*, **139**, 894–911, doi:10.1002/qj.1964.
- , Y. Hong, J. J. Gourley, M. Schwaller, W. Petersen, and J. Zhang, 2013b: Comparison of TRMM 2a25 products, version 6 and version 7, with NOAA/NSSL ground radar-based national mosaic QPE. *J. Hydrometeorol.*, **14**, 661–669, doi:10.1175/JHM-D-12-030.1.
- Kumar, P., and E. Foufoula-Georgiou, 1993: A multicomponent decomposition of spatial rainfall fields: 1. Segregation of large- and small-scale features using wavelet transforms. *Water Resour. Res.*, **29**, 2515–2532, doi:10.1029/93WR00548.
- , and —, 1994: Wavelet analysis in geophysics: An introduction. *Wavelets in Geophysics*, Academic Press, 1–43.
- , and —, 1997: Wavelet analysis for geophysical applications. *Rev. Geophys.*, **35**, 385–412, doi:10.1029/97RG00427.
- Kummerow, C. D., W. Barnes, T. Kozu, J. Shiue, and J. Simpson, 1998: The Tropical Rainfall Measuring Mission (TRMM) sensor package. *J. Atmos. Oceanic Technol.*, **15**, 809–817, doi:10.1175/1520-0426(1998)015<0809:TTRMMT>2.0.CO;2.
- , and Coauthors, 2001: The evolution of the Goddard Profiling Algorithm (GPROF) for rainfall estimation from passive microwave sensors. *J. Appl. Meteor.*, **40**, 1801–1820, doi:10.1175/1520-0450(2001)040<1801:TEOTGP>2.0.CO;2.
- , D. L. Randel, M. Kulie, N. Y. Wang, R. Ferraro, S. Joseph Munchak, and V. Petković, 2015: The evolution of the Goddard Profiling algorithm to a fully parametric scheme. *J. Atmos. Oceanic Technol.*, **32**, 2265–2280, doi:10.1175/JTECH-D-15-0039.1.
- Mallat, S., 2008: *A Wavelet Tour of Signal Processing: The Sparse Way*. Academic Press, 832 pp.
- Nesbitt, S. W., R. Cifelli, and S. A. Rutledge, 2006: Storm morphology and rainfall characteristics of TRMM precipitation features. *Mon. Wea. Rev.*, **134**, 2702–2721, doi:10.1175/MWR3200.1.
- Oliveira, R. A., R. C. Braga, D. A. Vila, and C. A. Morales, 2015: Evaluation of GPROF-SSM/S rainfall estimates over land during the Brazilian CHUVA-VALE campaign. *Atmos. Res.*, **163**, 102–116, doi:10.1016/j.atmosres.2014.11.010.
- Perica, S., and E. Foufoula-Georgiou, 1996: Linkage of scaling and thermodynamic parameters of rainfall: Results from mid-latitude mesoscale convective systems. *J. Geophys. Res.*, **101**, 7431–7448, doi:10.1029/95JD02372.
- Petković, V., and C. D. Kummerow, 2017: Understanding the sources of satellite passive microwave rainfall retrieval systematic errors over land. *J. Appl. Meteor. Climatol.*, **56**, 597–614, doi:10.1175/JAMC-D-16-0174.1.

- Petty, G. W., and K. Li, 2013: Improved passive microwave retrievals of rain rate over land and ocean. Part II: Validation and intercomparison. *J. Atmos. Oceanic Technol.*, **30**, 2509–2526, doi:10.1175/JTECH-D-12-00184.1.
- , and R. Bennartz, 2017: Field-of-view characteristics and resolution matching for the Global Precipitation Measurement (GPM) Microwave Imager (GMI). *Atmos. Meas. Tech.*, **10**, 745–758, doi:10.5194/amt-10-745-2017.
- Spencer, R. W., H. M. Goodman, and R. E. Hood, 1989: Precipitation retrieval over land and ocean with the SSM/I: Identification and characteristics of the scattering signal. *J. Atmos. Oceanic Technol.*, **6**, 254–273, doi:10.1175/1520-0426(1989)006<0254:PROLAO>2.0.CO;2.
- Tang, L., Y. Tian, and X. Lin, 2014: Validation of precipitation retrievals over land from satellite-based passive microwave sensors. *J. Geophys. Res. Atmos.*, **119**, 4546–4567, doi:10.1002/2013JD020933.
- TRMM, 2011a: TRMM Microwave Imager Hydrometeor profile L2 1.5 hours, V7. Goddard Earth Sciences Data and Information Services Center (GES DISC), accessed 23 April 2016, [https://disc.gsfc.nasa.gov/datacollection/TRMM\\_2A12\\_7.html](https://disc.gsfc.nasa.gov/datacollection/TRMM_2A12_7.html).
- , 2011b: TRMM Precipitation Radar rainfall rate and profile L2 1.5 hours, V7. Goddard Earth Sciences Data and Information Services Center (GES DISC), accessed 23 April 2016, [https://disc.gsfc.nasa.gov/datacollection/TRMM\\_2A25\\_7.html](https://disc.gsfc.nasa.gov/datacollection/TRMM_2A25_7.html).
- Whitcher, B., 2015: Waveslim: Basic wavelet routines for one-, two- and three-dimensional signal processing, version 1.7.5. R package, <https://CRAN.R-project.org/package=waveslim>.